Cronfa - Swansea University Open Access Repository

_____

This is an author produced version of a paper published in :
Computer Methods in Applied Mechanics and Engineering

Cronfa URL for this paper:

_____

Paper:

Lamine, S. & Edwards, M. Multidimensional upwind schemes and higher resolution methods for three-component two-phase systems including gravity driven flow in porous media on unstructured grids. _Computer Methods in Applied Mechanics and Engineering_

_____

Multidimensional Upwind Schemes and Higher Resolution Methods for Three-component Two-phase Systems Including Gravity Driven Flow in Porous Media on Unstructured Grids

Sadok Lamine[a,1,*], Michael G. Edwards[b,1]

[a]*Shell Global Solutions International. B.V., Kessler Park 1, 2288 GS Rijswijk, The Netherlands*
[b]*Zienkiewicz Centre for Computational Engineering (ZCCE), College of Engineering, Swansea University, Singleton Park, Swansea, SA2 8PP UK*

Abstract

Standard reservoir simulation schemes employ single-point upstream weighting for approximation of the convective fluxes when multiple phases or components are present. These schemes introduce both coordinate-line numerical diffusion and crosswind diffusion into the solution that is grid and geometry dependent.

Families of locally conservative multidimensional upwind schemes are presented for essentially hyperbolic three-component two-phase flow systems of conservation laws in porous media including counter current gravity flow on unstructured grids. The multidimensional methods employ cell-based tracing, which involves tracing characteristic wave directions over each control-volume subquadrant. The multidimensional methods reduce crosswind diffusion inherent in standard methods for convective flow approximation in porous media. The schemes are coupled with continuous Darcy-flux approximations resulting from the elliptic pressure equation on unstructured grids.

Characteristic upwind approximations are proposed and compared with the classical upstream weighting schemes for cases including gravity segregated flow. When dealing with systems of hyperbolic equations, upwind characteristic wave decomposition is used for wave tracing. The multidimensional upwind cell-based tracing formulations are designed for unstructured grids (and include structured grids by default) and are stable subject to conditions on the tracing direction and CFL number and satisfy a local maximum principle that ensures solutions are free of spurious oscillations.

Benefits of the resulting schemes are demonstrated for two-phase flow and a three-component two-phase flow system including gravity segregated flow. The multidimensional cell based schemes are shown to reduce crosswind diffusion induced by standard upwind methods, and prove to be particularly effectively when flow is strongly non-aligned with the grid, leading to improved resolution of numerical saturation and concentration fronts. Extension of higher order schemes to a three-component two-phase flow systems of conservation laws on unstructured grids is also presented, which provides a significant improvement in flow resolution for the system cases. Comparison is drawn between the methods.

---

[*]Corresponding author: Phone: 31-70447-7371

Email addresses: `sadok.lamine@shell.com` (Sadok Lamine), `m.g.edwards@swansea.ac.uk` (Michael G. Edwards)

---

1. Introduction

Standard reservoir simulation schemes employ single-point upstream weighting for convective flux approximation. These schemes rely upon upwind information that is determined according to the grid geometry. As a consequence, directional diffusion is introduced into the solution that is grid and geometry dependent. By definition, the single-point upstream weighting scheme defines the control volume face flux by using information that flows across the face. However, crucially when selecting this data, while the criterion is based on the sign of the wave velocity at the control volume face, the actual data is defined by wind dependent nearest neighbour coordinate values. In one dimension, this is sufficient to unambiguously define the scheme in terms of the incoming wave direction whereas in higher dimensions, the wave direction can be at an angle to the local grid lines, according to the wave velocity vector direction. The deficiency of the standard scheme is its failure to recognize from exactly where the wave is coming and consequently fail to use the genuine upwind data. The effect can be particularly important for cases where flow is across grid co-ordinate lines and is known as cross-wind diffusion [38, 6, 10, 41, 42, 25, 2, 45, 34].

In order to overcome cross-wind diffusion effects truly multidimensional upwinding schemes have been proposed in the literature. These methods include the corner transport upwinding (CTU) [10], the N-scheme [40, 23, 25] and the rotated grid H-box methods [7, 22] for Cartesian grids. The methods use characteristic information to determine the numerical fluxes via the tracing over control volumes. They are designed to monitor the average time evolution of the approximation to the solution within a complete grid cell rather than concentrating on the activity at the interfaces. A family of genuine multidimensional wave oriented upwind schemes was first introduced for reservoir simulation on structured quadrilateral grids in [15, 18] for miscible and two phase flow in porous media involving linear and nonlinear fluxes. A related method is presented in [27] for miscible gas injection in porous media on Cartesian grids. The formulation of these schemes is closely related to the uniform structure of the grid and requires further consideration in extending them to general unstructured grids. More recently, extension of multidimensional schemes to unstructured grids in two dimensions for linear and nonlinear fluxes for flow transport in porous media has been presented in [31, 28, 30] using a cell-vertex multidimensional *edge-based* tracing formulation, and in [32] using a cell-vertex multidimensional *cell-based* tracing formulation, and in [26] on cell centred unstructured grids.

However the fundamental multidimensional upwind schemes are not designed to overcome coordinate line oriented numerical diffusion, which can remain excessive when flow is parallel to local coordinate line directions and the methods remain formally first order. Higher order convection schemes continue to be developed for the essentially hyperbolic systems of reservoir simulation e.g. [6, 8, 19, 12, 13, 49, 47, 39, 11, 16, 29, 24, 36, 35] and references therein. These schemes require an extended support to obtain higher order accuracy and are constructed such that the solution remains free of spurious oscillations. These methods yield benefits in terms of improved front resolution and have been successfully demonstrated for a variety of multi-phase flow problems in reservoir simulation.

2

This paper presents;

i) Extension of cell-vertex multidimensional upwind schemes, with cell-based upwind tracing to two-phase and three-component two-phase flow systems, including gravity driven flow on unstructured grids.

ii) Extension of higher order methods to three-component two-phase flow systems on unstructured grids.

Method performance is demonstrated with the study of two-phase flow and a three component two-phase flow polymer flood system in two dimensions. The higher order methods provide a classical route towards improved resolution of flow fields and also make for an interesting comparison with the multidimensional schemes.

Multidimensional upwind schemes are made particularly attractive by their local and relatively small support when compared to higher order methods. The new multidimensional schemes upwind in the direction along which waves have traveled and are constructed to be locally conservative for any flux type linear or nonlinear. Conditions for stability, derived in [32] via positivity analysis, are employed componentwise in this work and yield results of improved resolution that are essentially free of spurious oscillations.

The schemes are coupled with continuous Darcy-flux approximations for transport [16] and maintain a single degree of freedom per control-volume per flow variable. Darcy-flux approximations are derived within a locally conservative flux-continuous full-tensor finite-volume scheme framework previously developed for the essentially elliptic component of the reservoir simulation system. The elliptic schemes are known as control-volume distributed multi-point flux approximation(CVD-MPFA) where flow variables and rock properties are assigned to the control-volumes of the grid and provide a consistent discretization of the porous medium pressure equation applicable to general geometry and permeability tensors on structured and unstructured grids, see e.g. [14, 37, 1, 33, 50] and references therein for further details of the Darcy flux approximation.

The new multidimensional and higher order schemes are formulated and applied to two-phase flow and a three component two-phase flow system that includes gravity on structured and unstructured grids.

The paper is organized as follows. After the introduction, the second section introduces the two-phase flow equations including gravity in two dimensions. The third section describes the discrete finite-volume formulation. The fourth section is devoted to the formulation of the multidimensional cell-based tracing schemes. Details of the three-component two-phase flow system is given in section 5 together with the eigenvalue decomposition. The extension of the multidimensional upwind scheme from two-phase flow to the three-component two-phase flow discrete system is also presented in section 5. The extension of higher order schemes to the three-component two-phase flow system on unstructured grids is given in section 6. Numerical results are presented in section 7 which illustrate the benefits of the new formulations compared to standard methods on structured and unstructured meshes. Conclusions are presented in section 8.

2. Flow Equations

We consider a multiphase flow system in the presence of gravity where capillary pressure and dispersion are neglected. The integral form of the multiphase flow continuity equations for N_p

phases, is written as

$$\int_{\Omega_{cv}} (\Psi \frac{\partial S_p}{\partial t} + \nabla \bullet \mathbf{V}_p) d\tau = m_p \tag{1}$$

for $p = 1, N_p$, where the integral is taken over a control-volume Ω_{cv}, $d\tau$ is a volume increment, Ψ is the porosity and where S_p, $\mathbf{V}_p$ and m_p are the pth phase saturation, Darcy velocity (defined below) and specified phase flow rate respectively. Since the pore volume must always be filled by the fluids present, this gives rise to the volume balance where saturations sum to unity viz; $\Sigma_{p=1}^{N_p} S_p = 1$. The momentum equations are defined through Darcy's law where the pth phase velocity is defined as $\mathbf{V}_p = f_p(\mathbf{V}_T - \Lambda \Delta \rho(S)g\mathbf{K}\nabla h)$. Here $f_p = \lambda_p/\Lambda$ is the fractional flow of phase p and is the ratio of phase mobility λ_p to total mobility Λ. Total mobility $\Lambda = \sum_{p=1}^{N_p} \lambda_p$, phase mobility $\lambda_p = k_{rp}/\mu_p$, and k_{rp}, μ_p and ρ_p are the respective phase relative permeability, viscosity and density. The density difference $\Delta \rho = \rho_p - \overline{\rho}$ where $\overline{\rho} = \sum_{p=1}^{N_p} \rho_p \lambda_p/\Lambda$ is the mean density. $\mathbf{V}_T$ is the total Darcy velocity defined by $\mathbf{V}_T = \sum_{p=1}^{N_p} \mathbf{V}_p$ which results in $\mathbf{V}_T = -\Lambda \mathbf{K}(\nabla \phi + \overline{\rho}g\nabla h)$. Here $\mathbf{K}$ is a diagonal or full elliptic Cartesian permeability tensor, ϕ is the pressure, $\nabla \equiv \partial_{x_i}$ is the gradient operator and h is the height.

For incompressible flow summation of Equation 4 over the N_p phases, together with volume balance (saturations sum to unity) yields the pressure equation in the form

$$\int_{\Omega_{cv}} \nabla \bullet \mathbf{V}_T d\tau = -\int_{\Omega_{cv}} \nabla \bullet \Lambda \mathbf{K}(\nabla \phi + \overline{\rho}g\nabla h) d\tau = M \tag{2}$$

where M is a specified mass flow rate which is zero away from any source or sink (well).

2.1. Two phase immiscible flow

In this work we consider two phase flow and three component two phase flow. The two phase water-oil flow equations are considered first, where suffix w denotes water phase and S_w is water saturation. In particular the water phase velocity is expressed in the fractional flow form $\mathbf{V}_w = f_w(S_w)(\mathbf{V}_T - (\rho_w - \rho_o)\lambda_o g\mathbf{K}\nabla h)$ where $f_w = f_w(S_w)$ is the water phase fractional flow, and total velocity $\mathbf{V}_T = -(\Lambda \mathbf{K}\nabla \phi + (\rho_w \lambda_w + \rho_o \lambda_o)g\mathbf{K}\nabla h)$. The resulting elliptic pressure equation for two phase flow is written as

$$-\int_{\Omega_{cv}} \nabla \bullet \Lambda \mathbf{K}\nabla \phi d\tau - \int_{\Omega_{cv}} \nabla \bullet (\rho_w \lambda_w + \rho_o \lambda_o)g\mathbf{K}\nabla h d\tau = M \tag{3}$$

In preparation for the finite-volume discretization, the velocity divergence is integrated over a control volume Ω_{cv} with surface $\partial\Omega_{cv}$ via the Gauss divergence theorem, and the water phase saturation equation is written as

$$\int_{\Omega_{cv}} \Psi \frac{\partial S_w}{\partial t} d\tau + \oint_{\partial\Omega_{cv}} \mathbf{V}_w \bullet \hat{\mathbf{n}} ds = m_w \tag{4}$$

Neumann boundary conditions apply on solid walls with zero normal flux. Inflow-outflow conditions apply at wells/boundaries where fluxes/pressures are prescribed. Pressure is prescribed at a minimum of one point for incompressible flow. Initial data in terms of saturation and pressure fields are also prescribed and water saturation is prescribed at injectors. Further details can be found in [3].

2.1.1. Fractional flow and characteristic wave velocity

The fractional flow (Buckley-Leverett) formulation [5] identifies the true hyperbolic nature of the phase continuity equations. Two phase incompressible flow in absence of capillary pressure is governed by a single scalar hyperbolic equation for saturation coupled together with the pressure equation; the saturation for oil is deduced from the volume balance equation, where the saturations sum to unity.

The water phase velocity $\mathbf{V}_w = f_w(\mathbf{V}_T - (\rho_w - \rho_o)\lambda_o g\mathbf{K}\nabla h)$ is now written in the form:

$$\mathbf{V}_w = f_w\mathbf{V}_T + \gamma\mathbf{V}_G \tag{5}$$

where $\mathbf{V}_T$ is the total velocity as before and

$$\mathbf{V}_G = g(\rho_o - \rho_w)\mathbf{K}\nabla h$$

denotes the spatial velocity due to gravity. Corey relative permeabilities are used with $k_{rp} = k_{rp}^o S_p^\zeta$ where k_{rp}^o is the endpoint value. The fractional flow is defined by:

$$f_w = \frac{\lambda_w(S)}{\Lambda(S)} = \frac{MS^\zeta}{MS^\zeta + (1-S)^\zeta} \tag{6}$$

where mobility ratio $M = \frac{k_{rw}^o/\mu_w}{k_{ro}^o/\mu_o}$ and the function γ corresponds to:

$$\gamma = \lambda_o f_w = \frac{\lambda_o(S)\lambda_w(S)}{\Lambda(S)} = \frac{M(1-S)^\zeta S^\zeta}{MS^\zeta + (1-S)^\zeta} \tag{7}$$

where $\zeta > 0$ defines the order of mobility, and the suffix w is omitted, and it will be understood that S denotes water saturation. The characteristic wave velocity is defined by

$$\mathbf{w}(S) = \frac{\partial f}{\partial S}\mathbf{V}_T + \frac{\partial \gamma}{\partial S}\mathbf{V}_G. \tag{8}$$

Upwinding is discussed in the convective flow formulation below and is performed according to the characteristic wave speed, defined by a discrete approximation of Eq.8. The standard scheme is well established [21] and provides physically consistent solutions.

3. Vertex Centered Finite Volume Discretisation

A vertex-centered finite volume approximation is used here. We refer to a grid comprised of triangles and/or quadrilateral cells with edges connected to grid vertices as the primal grid. A control-volume is constructed around each vertex j by connecting cell-centres to cell edge midpoints for all cells sharing a common vertex, which gives rise to a dual grid of polygons. Primal and dual (control-volume) grid segments are illustrated in Figure 1 with continuous and dashed lines respectively. The control-volume surrounding node j in Figure 1(a) has a bold dashed line. As a result of forming the dual grid, the primal cells are partitioned into subcells (3 for a triangle and 4 for a quadrilateral), where each subcell belongs to the control-volume of the vertex to which it is attached. Fluxes are defined cell-wise, first the elliptic continuous Darcy-fluxes are defined normal to each (dashed) subcell-face (from here on called a subface) inside the primal grid cells.

A flux-continuous control-volume distributed multi-point flux approximation (CVD-MPFA) finite-volume scheme is employed for the elliptic pressure equation, we refer to e.g. [14, 37, 20] for details of the elliptic approximation. Here we show how the elliptic approximation is coupled with the convective approximation. Using the Gauss divergence theorem Eq. 2 is written as a surface integral where

$$\int_{\Omega_{cv}} \nabla \bullet \mathbf{V}_T d\tau = \oint_{\partial\Omega_{cv}} \mathbf{V}_T \bullet d\mathbf{n} \tag{9}$$

and when applied over a control-volume comprised of discrete surface increments Eq. 9 is integrated over a discrete control-volume Ω_{cv} with boundary $\partial\Omega_{cv}$ comprised of surface increments termed subfaces. The integral is expressed as the sum of outward normal flux over each of the surface increments or subfaces of the control-volume Ω_{cv}. Two subfaces are associated with each field edge connected to the central vertex, and one subface for boundary edges. For example for the *key* edge connecting i and j in Fig. 1(b), one subface connects the lower triangle cell centre $\mathbf{x}_L$ to the edge mid-point $\mathbf{x}_e$, and the second subface connects the upper (quad) cell centre $\mathbf{x}_U$ to edge mid-point $\mathbf{x}_e$. Subfaces are shown as dashed lines in Fig. 1(a) which illustrate a control-volume perimeter, and in Fig. 1(c) which shows subfaces attached to the edge connecting i and j, that we label e. The lower and upper subfaces have local indices $k = 1$ and $k = 2$ respectively. Approximation of the lower subface integral $\int_{\mathbf{x}_L}^{\mathbf{x}_e} \mathbf{V}_T \bullet d\mathbf{n}$ is denoted by $\mathrm{F}_{T_{e,1}}$ and the upper subface integral $\int_{\mathbf{x}_e}^{\mathbf{x}_U} \mathbf{V}_T \bullet d\mathbf{n}$ is denoted by $\mathrm{F}_{T_{e,2}}$. Net divergence over a control-volume surrounding a primal grid vertex is then approximated by the sum of edge based accumulated fluxes, with approximation of the closed integral Eq. 9 given by

$$\sum_{e=1}^{N_{edV}} \sum_{k=1}^{N_e} \mathrm{F}_{T_{e,k}} = M_j \tag{10}$$

where $M_j = 0$ away from sources and sinks (or wells) and N_{edV} is the number of edges connected to the central vertex j, and N_e is the number of subfaces attached to edge e. The phase continuity equations (4) are coupled through the pressure equation (10).

In this work for convective multi-phase flow each normal subface flux is first used to determine a local upwind approximation. The resulting cell-wise convective approximations are then accumulated with respect to the primal cell edges to which the subfaces are connected, and finally control-volume divergence is formed as before, by summation of the edge based accumulated convective fluxes with sum over edges attached to the grid vertex. The approximation is expressed as follows:

Let N_{edV} be the total number of edges of the primal mesh connected to vertex j and τ_j the jth control-volume area. The semi-discrete finite volume form of Equation (4) (with phase velocity defined by Eq. 5) for multi-phase flow on unstructured grids is written as

$$\Psi_j \tau_j \frac{d}{dt} S_j + \sum_{e=1}^{N_{edV}} \sum_{k=1}^{N_e} [\mathrm{f}(S_{L_{e,k}}^n, S_{R_{e,k}}^n) F_{T_{e,k}}(\phi^{n+1}) + \gamma(S_{L_{e,k}}^n, S_{R_{e,k}}^n) F_{G_{e,k}}] = m_j, \tag{11}$$

where $F_{T_{e,k}}, F_{G_{e,k}}$ are the respective discrete flux approximations of total velocity flux and spatial gravity velocity flux c.f. Eq. 5, and as before k sums over the local number of subfaces attached to edge e. On boundaries $N_e = 1$ otherwise $N_e = 2$ in the field where two subcell faces join at

the edge midpoint, one from either side. Here $f(S_{L_{e,k}}^n, S_{R_{e,k}}^n)$ and $\gamma(S_{L_{e,k}}^n, S_{R_{e,k}}^n)$ have double arguments denoting numerical approximations of fractional flow and non-linear gravity terms, which are defined below via an upwind flux and $S_{L_{e,k}}^n, S_{R_{e,k}}^n$ are left and right hand states of the water phase saturation with respect to each subface k of edge e, and n denotes the time level of the variables.

The elliptic Darcy-flux comprised of the discrete total velocity flux $F_{T_{e,k}}$ and gravity flux $F_{G_{e,k}}$ is computed at a single quadrature point per subcell face [14], with sub-face index k and attached to edge $e(i,j)$. As before the index $k = 1, N_e$ loops over the connecting subfaces attached to edge e, where $N_e = 1$ at a boundary and $N_e = 2$ otherwise. m_j denotes the phase flow rate, which is prescribed at wells and is zero otherwise.

We note that;

(i) For the standard first order upwind formulation $S_{L_{e,k}}^n, S_{R_{e,k}}^n$ correspond to the left and right hand vertex control-volume values S_i^n, S_j^n of the saturation with respect to edge e.

(ii) In the case of the multi-dimensional formulation presented below, the values of $S_{L_{e,k}}^n, S_{R_{e,k}}^n$ will be defined by upwind wave tracing in subcells of the primal cells $k = 1, N_e$ that are attached to edge e, and will only correspond to the vertex values if the wave vector is aligned with the edge.

The phase continuity equations are coupled through the discrete pressure equation

$$\sum_{e=1}^{N_{edV}} \sum_{k=1}^{N_e} F_{T_{e,k}}(\phi^{n+1}) = M_j \tag{12}$$

The system Equations 11 and 12 are solved sequentially, Equation 12 is first solved implicitly for pressure (i.e. total velocity flux is a function of ϕ^{n+1}) while Equation 11 is solved explicitly in this formulation for saturation. Thus the formulation developed here is implicit pressure explicit saturation (IMPES). Time integration is illustrated with the explicit Forward Euler method, although a maximum principle preserving Runge-Kutta method is equally applicable [9]. The focus here is on the spatial discretization. The discrete cell based finite-volume scheme is now written as:

$$\Psi_j \tau_j (S_j^{n+1} - S_j^n) + \Delta t \sum_{e=1}^{N_{edV}} \sum_{k=1}^{N_e} [f(S_{L_{e,k}}^n, S_{R_{e,k}}^n) F_{T_{e,k}}(\phi^{n+1}) + \gamma(S_{L_{e,k}}^n, S_{R_{e,k}}^n) F_{G_{e,k}}] = m_j, \tag{13}$$

Characteristic Upwind Scheme

To simplify notation, we denote the numerical Darcy phase flux of Eq.13 by $\mathfrak{V}_{e,k}(S_{L_{e,k}}^n, S_{R_{e,k}}^n)$ where now

$$\mathfrak{V}_{e,k}(S_{L_{e,k}}^n, S_{R_{e,k}}^n) = [f(S_{L_{e,k}}^n, S_{R_{e,k}}^n) F_{T_{e,k}}(\phi^{n+1}) + \gamma(S_{L_{e,k}}^n, S_{R_{e,k}}^n) F_{G_{e,k}}], \tag{14}$$

then the vertex centered finite volume discretization of Eq. 13 on unstructured grids takes the simpler form:

$$\Psi_j \tau_j (S_j^{n+1} - S_j^n) + \Delta t \sum_{e=1}^{N_{edV}} \sum_{k=1}^{N_e} \mathfrak{V}_{e,k}(S_{L_{e,k}}^n, S_{R_{e,k}}^n) = m_j, \tag{15}$$

Next we define the semi-analytical Darcy phase flux by $\mathfrak{V}_{e,k}(S)$ with single argument, by

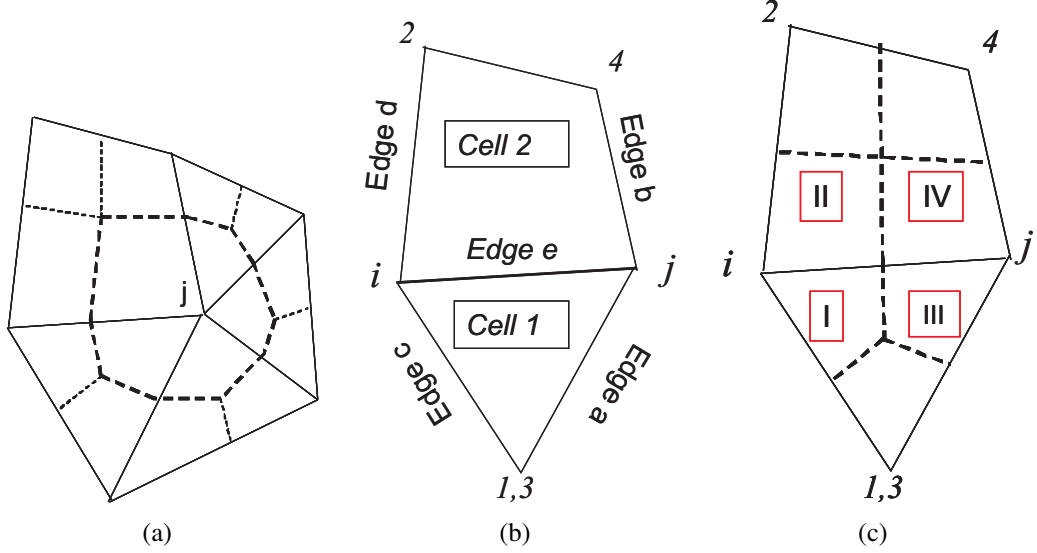$$\mathfrak{V}_{e,k}(S) = f(S) F_{T_{e,k}}(\phi^{n+1}) + \gamma(S) F_{G_{e,k}}, \tag{16}$$

Figure 1: (a) Control-volume j is closed loop (dashed line) around vertex j (b) compact stencil for flux approximation, lower and upper cells sharing edge e with vertices i and j (c) subcells that contribute to upwind wave tracing and approximation I-IV. E.g. if subcell flux component along edge e is positive (convention flow from i to j), wave path tracing will be defined via flux ratios in subcell I and/or subcell II depending upon signs of respective subcell component fluxes. Subfaces of vertex control-volumes have dashed lines. Lower and upper subfaces (k=1,2) connect cell mid-points to the common edge e midpoint.

where $f(S)$ and $\gamma(S)$ are the respective analytical fractional flow and gravity non-linearity terms. Then the characteristic wave velocity resolved on the kth subface is given by

$$w_{e,k}(S) = \frac{\partial f}{\partial S} F_{T_{e,k}}(\phi^{n+1}) + \frac{\partial \gamma}{\partial S} F_{G_{e,k}}, \tag{17}$$

which is used to determine the upwind sign in the definition of the upwind flux. The characteristic upwind flux approximation used here is defined by:

$$\mathfrak{V}_{e,k}(S^n_{L_{e,k}}, S^n_{R_{e,k}}) = \begin{cases} \mathfrak{V}_{e,k}(S^n_{L_{e,k}}) & \text{if } w_{e,k}(S) > 0, \text{ for } S \in [S_{L_{e,k}}, S_{R_{e,k}}], \\ \mathfrak{V}_{e,k}(S^n_{R_{e,k}}) & \text{if } w_{e,k}(S) < 0, \text{ for } S \in [S_{L_{e,k}}, S_{R_{e,k}}], \\ \mathfrak{V}^{LLF}_{e,k} & \text{otherwise} \end{cases} \tag{18}$$

where at sonic points, a Local Lax Friedrichs (LLF) flux approximation $\mathfrak{V}^{LLF}_e$ provides a local entropy satisfying flux that disperses expansion shocks [44, 21]. The sonic loci are determined using a test for the change of sign in $w_{e,k}$ evaluated at the left and right states of the local Riemann problem. Practically, the LLF approximation is adopted when $w_{e,k}(S_{L_{e,k}}) < 0$ and $w_{e,k}(S_{R_{e,k}}) > 0$ which has proved effective and minimises additional dissipation [17]. The Local Lax Friedrichs numerical flux is written as:

$$\mathfrak{V}^{LLF}_{e,k} = \frac{1}{2}[(\mathfrak{V}_{e,k}(S^n_{L_{e,k}}) + \mathfrak{V}_{e,k}(S^n_{R_{e,k}})) - \max_{[S^n_{L_{e,k}}, S^n_{R_{e,k}}]} \mid w_{e,k} \mid (S^n_{R_{e,k}} - S^n_{L_{e,k}})]. \tag{19}$$

Finally we note that this flux is defined cell-wise on each subface with definition of wave velocity in cells (subface indices $k = 1$ and $k = 2$) attached to edge e respectively. The flux

reduces to a subface first order upwind method whenever $\mathfrak{V}_{\mathfrak{e},\mathfrak{k}}(S^n_{L_{e,k}}) = \mathfrak{V}_{\mathfrak{e},\mathfrak{k}}(S^n_i)$ and $\mathfrak{V}_{\mathfrak{e},\mathfrak{k}}(S^n_{R_{e,k}}) = \mathfrak{V}_{\mathfrak{e},\mathfrak{k}}(S^n_j)$. However the multi-dimensional method uses directional upwind interpolated data to define $S_{L_{e,k}}, S_{R_{e,k}}$, as described below.

4. Locally Conservative Multi-Dimensional Cell-Based Upwind Approximations

The standard first order (single-point upstream weighting) scheme defines the control volume face flux using the sign of the wave (characteristic or flow) velocity at the control volume face, with the actual data defined by the nearest neighbour coordinate value. While this is sufficient in one dimension to unambiguously define the flux in terms of the incoming wave information, in higher dimensions the wave direction is defined by the angle of the wave velocity vector.
Thus the standard scheme can fail to recognize the wave vector direction and consequently fail to use the genuine upwind data. The actual physical wave direction which can be at some angle to the coordinate lines, and capturing genuine upwind data requires that the scheme has the ability to use data within a cell radius of each control-volume face. On a structured quadrilateral grid, a genuine multidimensional scheme will increase the support-stencil from five nodes to nine nodes in two dimensions, completing the square of nodes surrounding the central node. This enhances stability and permits a unit directional CFL number ([10, 15]) on structured grids.
The main idea of the multidimensional scheme is to define the upwind flux approximation by tracing back from the control-volume subface along the two-dimensional characteristic or wave vector path to the point of intersection with the upwind adjacent coordinate lines (adjacent edges of the cell) whenever possible and thereby use appropriately interpolated data to define the upwind scheme. The approximation of the wave vector direction is an important component of the multi-dimensional method, since this is used to define the tracing paths. Here tracing is performed with respect to the control-volume subface flux flow paths defined below. In this section, two key issues are addressed namely:

1. The definition of the upwind direction based on the local wave velocity defined over the subcells and
2. The choice of the weighting coefficients to minimize the cross-wind diffusion while preserving positivity.

4.1. Formulation using data

First, we consider two phase flow and present a family of genuinely multidimensional cell-based finite-volume schemes on unstructured grids using a data based formulation. Consider the key edge e and the adjacent cells sharing the edge as shown in Figure 2. Let e_1 and e_2 denote the control volume sub-faces connected to edge $e(i,j)$ oriented from i to j belonging to the adjacent cells $cell_1$ and $cell_2$. The left and right states used at the integration point of the control volume sub-faces connected the edge $e(i,j)$ are defined by tracing back to the left and right right hand edges of the cell and using data interpolated along the respective edges. The actual point of intersection with each edge is determined by the path along which the data travels. The characteristic flow paths are determined from subface fluxes defined in the cells, and are therefore determined at a finer scale than previous schemes which use edge assembled fluxes [31, 30]. Stability of the schemes will require limiting conditions be placed on the local flow angles in the cells [32].
We now give the general form of the left and right hand data relative to the subface connected

to the mid-point of key edge e, in terms of dimensionless interpolant parameters $\xi_{e,k}$ (left hand adjacent cell edge), $\eta_{e,k}$ (right hand adjacent cell edge) where $0 \leq \xi_{e,k} \leq 1$ and $0 \leq \eta_{e,k} \leq 1$. This convention is adopted for each subface $k = 1, N_e$ relative to the key edge $e(i, j)$. On triangular cells the data values are defined by:

$$\begin{aligned}
S_{L_{e,1}}^n &= (1 - \xi_{e,1})S_i^n + \xi_{e,1}S_1^n, \\
S_{R_{e,1}}^n &= (1 - \eta_{e,1})S_j^n + \eta_{e,1}S_1^n;
\end{aligned} \qquad (20)$$

and on quadrilateral cells by:

$$\begin{aligned}
S_{L_{e,2}}^n &= (1 - \xi_{e,2})S_i^n + \xi_{e,2}S_2^n, \\
S_{R_{e,2}}^n &= (1 - \eta_{e,2})S_j^n + \eta_{e,2}S_4^n.
\end{aligned} \qquad (21)$$

The interpolant parameters $(\xi_{e,k}, \eta_{e,k})$ are locally defined according to flow angle, by wave tracing using the subcell sub-face fluxes as indicated in Figure 2. Thus the data interpolant takes account of the true wave direction, giving rise to a multidimensional approximation when used in the flux. Limiting required for stability is given below, with respect to a local frame of reference along each edge of the cell in question.

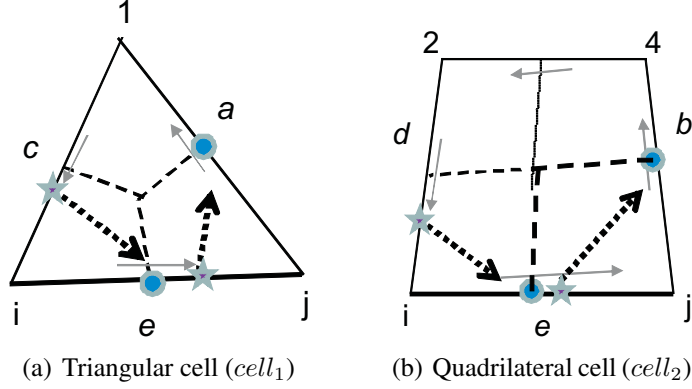(a) Triangular cell ($cell_1$)   (b) Quadrilateral cell ($cell_2$)

Figure 2: Local tracing: local interpolant points are indicated by a star and tracing streamlines are shown in dotted arrows. Grey arrows illustrate sub-cell fluxes calculated at the centre of cell edges.

In the following, we present the method with respect to triangular cell, labelled cell 1, the suffix (e, k) is replaced by $(e, 1)$. Extensions of the formulations to a quadrilateral cell, labelled here as cell 2 is done similarly.

4.2. Nonlinear Multi-dimensional Flux

We have developed both multi-dimensional upwind data and flux formulations. Here we present the multi-dimensional upwind flux formulation as a two step process:

4.2.1. Step I: The flux interpolant

where we define the generalized flux for the triangular cell 1 by:

$$\begin{aligned}
\mathfrak{V}_{e,k}(S_{L_{e,1}}^n) &= (1 - \xi_{e,1})\mathfrak{V}_{e,k}(S_i^n) + \xi_{e,1}\mathfrak{V}_{e,k}(S_1^n), \qquad (22) \\
\mathfrak{V}_{e,k}(S_{R_{e,1}}^n) &= (1 - \eta_{e,1})\mathfrak{V}_{e,k}(S_j^n) + \eta_{e,1}\mathfrak{V}_{e,k}(S_1^n). \qquad (23)
\end{aligned}$$

10

4.2.2. Step II: Limiting Strategy Tracing with Characteristic Velocity

The tracing step is common to both the multi-dimensional upwind data and flux formulations, and is described here for a positive incoming wave. The resolved aqueous phase characteristic wave speed at the subface of cell 1 attached to edge $e(i, j)$ is:

$$W_{e,1} = \begin{cases} \frac{\mathfrak{V}_{e,1}(S_j) - \mathfrak{V}_{e,1}(S_i)}{S_j - S_i}, & \mid S_j - S_i \mid \geq \epsilon; \\ w_{e,1}(S), & \mid S_j - S_i \mid \leq \epsilon. \end{cases} \tag{24}$$

which is a discrete approximation of the wave speed of Eq. 8 resolved along the control-volume subface normal, defined by the Rankine-Hugoniot shock speed for any discrete difference in edge vertex saturations (where ϵ is a tolerance), with Darcy flux $\mathfrak{V}_{e,1}$ defined by Equation (16), otherwise the characteristic wave speed $w_{e,1}$ is defined by Equation (17).

Note here that the resultant characteristic wave tracing direction is determined by the ratio of wave speeds resolved on normals of respective subfaces attached to edges e and c in this case. The subface speed $W_{c,1}$ associated with edge c of cell 1 has an equivalent definition to Equation (24), using data associated with edge c.

Thus for an incoming positive wave, the flux ratio $R_{e,1}$ becomes:

$$R_{e,1} = \frac{W_{c,1}}{W_{e,1}}, \tag{25}$$

and the weighting factor is written as:

$$\xi_{e,1} \leq \beta \min(1, R_{e,1}) \text{ with } \beta = \begin{cases} \frac{1}{2} & \text{if } W_{c,1} < 0, \\ 1 & \text{otherwise} \end{cases} \tag{26}$$

where the above limiting conditions, together with the CFL condition ensure positivity (local discrete maximum principle) and are derived in [32]. The right hand flux is defined in terms of $\eta_{e,1}$ in analogous fashion for an incoming negative wave.

5. Three-component two-phase flow system

The integral conservation equations for a polymer flood three component two phase flow system over Ω in the absence of source and sink terms are written as:

$$\int_\Omega \Psi \frac{\partial \mathbf{S}}{\partial t} + \oint_{\partial \Omega_{cv}} \mathbf{F}(\mathbf{S}) \mathrm{d}L = \mathbf{0}, \tag{27}$$

where $\mathbf{F} = (\mathbf{V} \cdot \hat{\mathbf{n}}, C\mathbf{V} \cdot \hat{\mathbf{n}})^t$ is the column flux vector, $\mathbf{S}$ is the vector of conservative variables defined by $\mathbf{S} = (S, SC)^T$ and $\hat{\mathbf{n}} \mathrm{d}L$ is the outward normal surface increment of the control-volume boundary. In this section, S denotes the miscible phase saturation and C the component concentration in the miscible phase, here the aqueous phase, $\mathbf{V} = \mathbf{V}(\mathbf{S})$ refers to the Darcy velocity of the aqueous phase defined by:

$$\mathbf{V} = f(\mathbf{S})\mathbf{V}_T + \gamma(\mathbf{S})\mathbf{V}_G \tag{28}$$

and the velocity resolved along direction $\hat{\mathbf{n}}$ is denoted $V(\mathbf{S}) = \mathbf{V} \cdot \hat{\mathbf{n}}$. The fractional flow takes the same form as in Equation (6) where the water viscosity is now a function of concentration and is

set to $\mu_w = 0.5 + C$. Thus the water phase is now a function of saturation and concentration.

Characteristic Upwind Approximation

We use a characteristic decomposition upwind scheme. The system is first decomposed into characteristic form. Decomposition is performed via a local transformation with respect to the control volume sub-face k attached to edge e

$$\Delta \mathbf{S} = \mathbf{R}_{e,k} \Delta \mathbf{U}, \tag{29}$$

where $\mathbf{R}_e$ is the matrix of right eigenvalues of the system Jacobian matrix $A = \frac{\partial \mathbf{F}}{\partial \mathbf{S}}$ and the matrix of eigenvalues $\Gamma_{e,k}$ is defined via

$$\Gamma_{e,k} = \mathbf{R}_{e,k}^{-1} \mathbf{A}_{e,k} \mathbf{R}_{e,k} \tag{30}$$

and $\Delta \mathbf{S}$, $\Delta \mathbf{U}$ represent the respective conservative and characteristic variable increments. The matrix of discrete eigenvalues $\Gamma_{e,k}$ is written as

$$\boldsymbol{\Gamma}_{e,k} = \begin{bmatrix} \frac{\partial V(\mathbf{S})}{\partial S} & 0 \\ 0 & \frac{V(\mathbf{S})}{S} \end{bmatrix}. \tag{31}$$

and the eigenvector transformation matrix $\mathbf{R_{e,k}}$ is defined by:

$$\mathbf{R_{e,k}} = \begin{bmatrix} 1 & \frac{\partial V(\mathbf{S})}{\partial C} \\ C & C\frac{\partial V(\mathbf{S})}{\partial C} + S(\frac{V(\mathbf{S})}{S} - \frac{\partial V(\mathbf{S})}{\partial S}) \end{bmatrix}. \tag{32}$$

The upwind scheme is in effect applied to each characteristic wave component and the discrete system is recomposed into a conservative form. The numerical flux corresponding to the control volume k attached to edge e is defined by:

$$\mathbf{F}(\mathbf{S_{L_{e,k}}}, \mathbf{S_{R_{e,k}}}) = \frac{1}{2}[\mathbf{F}(\mathbf{S_{L_{e,k}}}) + \mathbf{F}(\mathbf{S_{R_{e,k}}}) - \mathbf{R} \mid \boldsymbol{\Gamma_{e,k}} \mid \mathbf{R^{-1}}(\mathbf{S_{R_{e,k}}} - \mathbf{S_{L_{e,k}}})], \tag{33}$$

In the presence of stagnation points or if equal eigenvalues are detected (in which case, $\mathbf{R_{e,k}}$ becomes singular), a LLF-Rusanov flux approximation is applied locally [17]. The approximate flux will then take the LLF-Rusanov form:

$$\mathbf{F}(\mathbf{S_{L_{e,k}}}, \mathbf{S_{R_{e,k}}}) = \frac{1}{2}[\mathbf{F}(\mathbf{S_{L_{e,k}}}) + \mathbf{F}(\mathbf{S_{R_{e,k}}}) - \mid \boldsymbol{\Gamma_e^{RU}} \mid (\mathbf{S_{R_{e,k}}} - \mathbf{S_{L_{e,k}}})], \tag{34}$$

where

$$\mid \Gamma^{RU} \mid = \max_{[\mathbf{S}_L, \mathbf{S}_R]} \max_m \mid \Gamma_{e,k}^m(\mathbf{S}) \mid \mathbf{I}, \tag{35}$$

where $\Gamma_{e,k}^m$ is the mth diagonal entry of the 2×2 matrix $\Gamma_{e,k}^{RU}$. First order reconstruction corresponds with $\mathbf{S}_{L_{e,k}} = \mathbf{S}_i$ and $\mathbf{S}_{R_{e,k}} = \mathbf{S}_j$.

The vertex centered finite volume approximation of Equation (27) with respect to control volume j then takes the form

$$\Psi_j \tau_j \frac{\mathbf{S}_j^{n+1} - \mathbf{S}_j^n}{\Delta t} + \sum_{e=1}^{N_{edV}} \sum_{k=1}^{N_e} \mathbf{F}(\mathbf{S_{L_{e,k}}}, \mathbf{S_{R_{e,k}}}) \triangle L_{e,k} = 0, \tag{36}$$

where $\mathbf{F}(\mathbf{S_{L_{e,k}}}, \mathbf{S_{R_{e,k}}})\triangle L_{e,k}$ denotes the discrete cell-based Darcy flux system vector of Eq's. 33,34, where

$$\mathbf{F}(\mathbf{S_{L_{e,k}}})\triangle L_{e,k} = [\mathfrak{V}_{e,k}(\mathbf{S_{L_{e,k}}}), C_{e,k}\mathfrak{V}_{e,k}(\mathbf{S_{L_{e,k}}})]^t \tag{37}$$

is evaluated at the sub-face k of length $\triangle L_{e,k}$ attached to edge e. The flux $\mathbf{F}(\mathbf{S_{R_{e,k}}})\triangle L_{e,k}$ has an equivalent definition in terms of $\mathbf{S_{R_{e,k}}}$ and the eigenvectors and eigenvalues are corresponding subface normal resolved quantities. In the system case $\mathfrak{V}_{e,k}(\mathbf{S})$ is a function of saturation and concentration. The multidimensional data approximation of $\mathbf{S_{L_{e,k}}}, \mathbf{S_{R_{e,k}}}$ is described in the section below. The CFL condition now applies with respect to the maximum eigenvalue of the system.

5.1. Three component two-phase flow multidimensional upwind tracing scheme

In this section, the multidimensional cell-based schemes presented above for two phase flow are extended to the system of conservation laws, and involve componentwise multidimensional data reconstructions with respect to the subfaces k attached to key edge e.

Primitive Variable Tracing

The multidimensional method used here involves tracing on the characteristic wave directions defined by the eigenvalues of the system. This is achieved using the resolved wave speeds analogous to the scalar case.

For the saturation variable, the Rankine-Hugoniot wave speed $W_{e,1}$ is used as described in section 4 above, which corresponds to subface normal resolution of the first eigenvalue $\frac{\partial V(\mathbf{S})}{\partial S}$.

For the concentration, an analogous tracing is employed, now using an approximation of the subface normally resolved second eigenvalue corresponding to $\frac{V(\mathbf{S})}{S}$, with discrete approximation defined by $\mathfrak{V}_{e,1}/S$.

The left and right cell-based multidimensional saturation and concentration reconstructions with respect to the subface in cell 1 attached to key edge e, are written as:

$$\mathbf{S}_{L_{e,1}} = \mathbf{S}_i + \mathbf{P}_c \xi_{e,1} \mathbf{\Delta C}_{i1}, \tag{38}$$

$$\mathbf{S}_{R_{e,1}} = \mathbf{S}_j + \mathbf{P}_a \eta_{e,1} \mathbf{\Delta C}_{j1}, \tag{39}$$

where $\mathbf{C} = (S, C)^T$ is the vector of primitive variables, $\mathbf{P}$ is the transform matrix between conservative and primitive variables and the tensors of weighting factors $\xi_{e,1}$ and $\eta_{e,1}$ are diagonal matrices, with components defined by the limited tracing angles following section 4.2.2, using the above resolved system wave speeds. This completes the definition of the multidimensional characteristic reconstructions. Note in each tracing case that $\mathbf{S}_{L_{e,1}}$ and $\mathbf{S}_{R_{e,1}}$ is now substituted in Eq's.33,34,36 to complete the definition of the multidimensional scheme.

6. Higher Resolution Reconstruction for Systems

The higher order scheme uses extended support with respect to an edge, with reconstructed gradients defined by edge slopes and trace-back from the left edge vertex and trace-forward from right edge vertex to construct gradients in cells attached to respective edge vertices, we refer to [16, 29**?**] for details. Slope limiters then force a local maximum principle which prevents spurious

oscillations as described in [16, 29?]. For systems higher order reconstruction is defined by

$$\mathbf{S}_{L_{e,1}} \;=\; \mathbf{S}_i + \mathbf{R}_{e,k}\mathbf{\Phi}^+{}_{e,k}\mathbf{R}_{e,k}^{-1}\mathbf{\Delta S}_e, \tag{40}$$

$$\mathbf{S}_{R_{e,1}} \;=\; \mathbf{S}_j - \mathbf{R}_{e,k}\mathbf{\Phi}^-{}_{e,k}\mathbf{R}_{e,k}^{-1}\mathbf{\Delta S}_e, \tag{41}$$

where $\mathbf{\Delta S}_e = \mathbf{S}_j - \mathbf{S}_i$ and $\mathbf{\Phi}^+{}_{e,k}, \mathbf{\Phi}^-{}_{e,k}$ are column vectors of slope limiters [48, 4]. For systems the respective slope limiter components apply to ratios of characteristic gradients [13]. The vector of characteristic gradients at edge e is defined by $\mathbf{R}_{e,k}^{-1}\mathbf{\Delta S}_e$. The limiter vector $\mathbf{\Phi}^+{}_{e,k}$ is a function of the ratio of respective trace-back characteristic gradient components divided by the respective components of characteristic gradients at edge e. The limiter vector $\mathbf{\Phi}^-{}_{e,k}$ is a function of the ratio of respective trace-forward characteristic gradient components divided by the respective components of characteristic gradients at edge e. Standard limiters can be used, here we use the Fromm limiter [46], formulated for general grids as in [29].

Referring to the characteristic increments $\mathbf{\Delta U}$, we illustrate the limiter with respect to the component variable U and define the difference in U over the edge e Fig.3, as

$$\Delta U_{ji} = U_j - U_i \tag{42}$$

where it is now understood that ΔU_{ji} with a double suffix denotes a difference in U. Referring to Fig.3 the left and right states U_L and U_R at the midpoint of the *key* edge e (joining vertices i and j) are defined as follows: the left state

$$U_L = U_i + \frac{1}{2}\Phi^+\Delta U_{ji}, \tag{43}$$

where $\Phi^+ = \Phi(\mathbf{r}_{ji}^+)$ is a function of the directional gradient ratio

$$r_{ji}^+ = \frac{\Delta U_{iu}/\Delta r_{iu}}{\Delta U_{ji}/\Delta r_{ji}}. \tag{44}$$

between i to j, and u to i, Fig. 3. Similarly the right state

$$u_R = U_j - \frac{1}{2}\Phi^-\Delta U_{ji}, \tag{45}$$

where $\Phi^- = \Phi(\mathbf{r}_{ji}^-)$ is a function of directional gradient ratio

$$r_{ji}^- = \frac{\Delta U_{dj}/\Delta r_{dj}}{\Delta U_{ji}/\Delta r_{ji}}. \tag{46}$$

between j to d, and i to j, Fig. 3. Directional gradients are constructed by extrapolating along the *key* edge defined by vector $\Delta \mathbf{r}_{ji}$ in the respective upstream and downstream directions, to the indicated points u and d respectively, see arrows in Fig. 3. The corresponding component limiter is written as

$$\Phi(r) = max(0, min(2r, 2, \frac{\Delta r_{iu} + \Delta r_{ji}r}{\Delta r_{iu} + \Delta r_{ji}})), \tag{47}$$

14
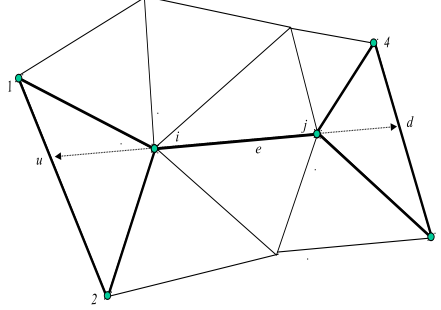
(a)

Figure 3: Higher Order Support: Slope limiters are reconstructed from edge gradient and respective left(right) hand triangle gradient for left(right) state. If the left(right) hand cell is a quadrilateral, such as the dashed line quad attached to j, then it is decomposed into 2 triangles and interpolation takes place on the resulting triangle attached to j.

where the distance weightings are indicated in Fig. 3, and the limiter reduces to the Fromm limiter on a uniformly spaced mesh. The vertex centered higher resolution finite-volume approximation of Equation (27) with respect to control volume j then takes the form

$$\Psi_j \tau_j \frac{\mathbf{S}_j^{n+1} - \mathbf{S}_j^n}{\Delta t} + \sum_{e=1}^{N_{edV}} \sum_{k=1}^{N_e} \mathbf{F}(\mathbf{S}_{\mathbf{L}_{e,k}}, \mathbf{S}_{\mathbf{R}_{e,k}}) \triangle L_{e,k} = 0, \tag{48}$$

where $\mathbf{F}(\mathbf{S}_{\mathbf{L}_{e,k}}, \mathbf{S}_{\mathbf{R}_{e,k}}) \triangle L_{e,k}$ denotes the discrete cell-based Darcy flux (defined by Eq's. 33,34 and 37) evaluated at the sub-face k of length $\triangle L_{e,k}$ attached to edge e, and the higher resolution data of Eq. 40 is used in the flux of Eq's. 33,34 and 37. Again the CFL condition applies with respect to the maximum eigenvalue of the system.

7. Results

Five cases are presented. Case 1 involves two-phase channel flow with a near flux. Case 2 involves two-phase flow with gravity. Cases 3 to 5 involve three-component two-phase flow; case 3 involves channel flow with a uniform full-tensor permeability field. Case 4 involves channel flow in a heterogeneous domain with meandering high permeability channels. Case 5 involves gravity segregation. Normalised time is expressed in pore volumes injected (PVI).

15
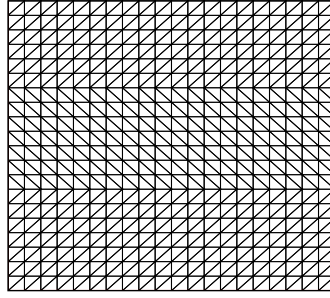
(a) Zigzag Grid

Figure 4: (a) 41x41 Zigzag Triangular Grid

A consistent elliptic Darcy flux is used in all cases, so that any grid induced errors are due to the convective flux approximation. The first case involves a linear flux so that data tracing and flux tracing are identical. The multidimensional flux of Eq. 22 is used for the scalar case 2. For the system results, characteristic tracing is used, with reconstruction of conservative variables via the primitive variables Eq. 38, which was found to be slightly more effective than characteristic variables in case 2. We have used flux of multidimensional data for the system cases, which is a more natural choice for systems.

7.1. CASE 1: Uniform flow on a zigzag grid

The first case involves uniform inflow with a linear flux. The challenge is to capture the discontinuity which is convected across the domain on a zigzag triangular grid shown in Fig. 4.
The standard first order method result computed on a Cartesian grid is shown in Fig. 5(a), and the standard first order result computed on the zigzag triangular grid is shown in Fig. 5(b). The standard first order result of Fig. 5(b) clearly shows a grid orientation effect that is induced by the cross-wind diffusion inherent in the single-point upwind scheme on the zigzag grid. The multidimensional scheme result, Fig. 5(c) shows that the multidimensional method clearly reduces the grid orientation effect. While the fundamental multidimensional scheme reduces cross-wind diffusion, this case also shows that the multidimensional scheme is first order and does not reduce coordinate aligned diffusion, as is seen by comparison with standard first order scheme on a Cartesian grid, that is aligned with the uniform flow direction, Fig. 5(a). The higher order method yields a significant improvement in flow resolution, Fig. 5(d). These results are consistent with the respective definitions of the first order multi-dimensional method, and the high-order method.

7.2. CASE 2: Two-phase flow gravity segregation

The second test case involves gravity driven two-phase flow. Quadratic relative permeabilities are assumed with $\zeta = 2$. The mobility ratio is set to unity. The permeability tensor is assumed to be diagonal isotropic.
The initial condition consists of an oil lens sitting on top of a shale barrier, in an otherwise gas filled reservoir, with solid walls at the sides and top boundaries. Pressure is specified on the lower boundary. In the absence of the shale barrier, the problem essentially involves flow with an infinite gravity number. Note that the two-phase flow formulation presented applies equally to water and
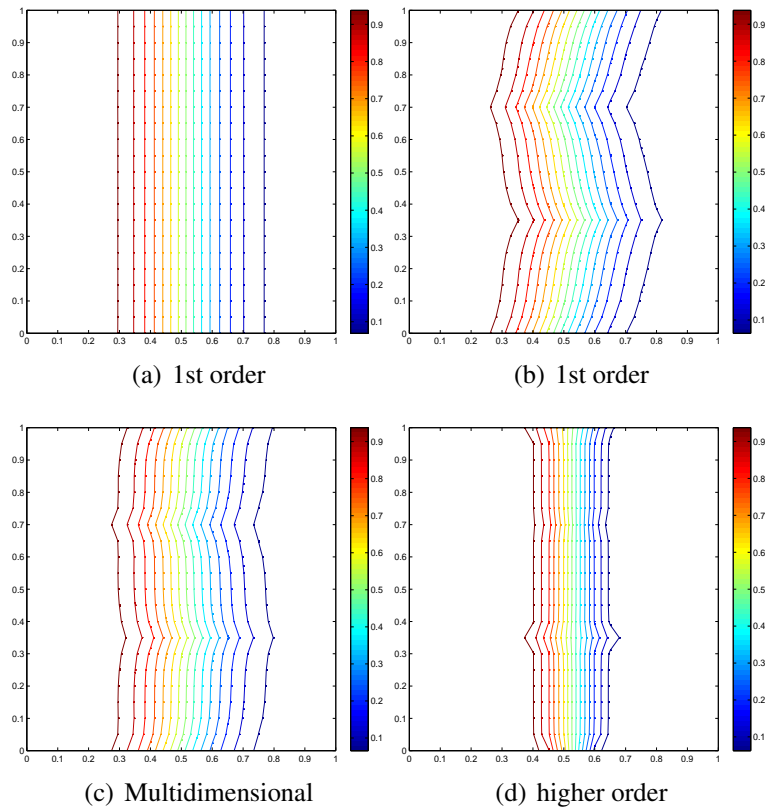
16

Figure 5: (a) Standard First order on a 41x41 Cartesian mesh. Results on 41x41 Zigzag Grid: (b) Standard First order. (c) Multidimensional First order. (d) Higher order.

oil and other two-phase combinations such as oil and gas.

The boundaries and initial interface are shown in Figure 6. Oil saturations are shown at the same
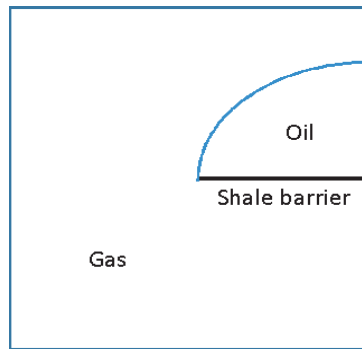

Figure 6: Case 2: Initial Conditions

output time 0.25 pore volumes injected (PVI) where the shock due to the downward moving heavier oil phase has formed followed by the Buckley Leverett expansion. A CFL of 0.45 is used for the first order method. The time step is reduced by a factor 2 for higher order results. The reference solution is computed on a uniform 65x65 Cartesian grid using standard higher order and shown in Figure 7. The methods are tested on a coarse unstructured quadrilateral grid shown in Figure 8(a) and compared with the reference solution in Figure 7.

The standard first order method results on the unstructured grid shows a smeared front Figure 8(b).

The multidimensional method using characteristic tracing Figure 8(c)) provides oscillation free results with slightly sharper resolution of the saturation front, particularly in regions where cross-flow is important, when compared with standard first order. The results show that even on a very coarse, poor quality unstructured grid, some improvement is still gained by the higher order method, where the results show there is less spread in shock front resolution Figure 8(d) versus Figure 8(b), and while the multi-dimensional method has smaller impact, the result still shows less spread of the front Figure 8(c) versus Figure 8(b), and Figure 8(c) shows the trend of Figure 8(d).
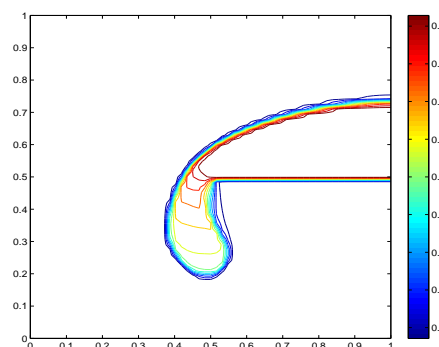
(a) Reference Solution

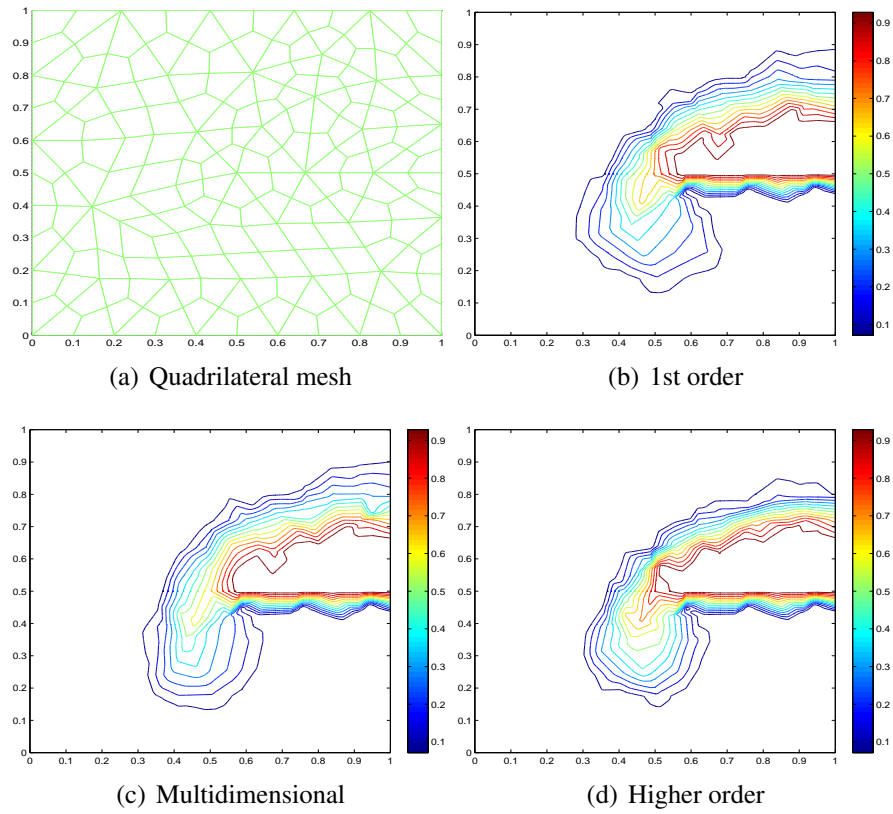Figure 7: (a)Reference Solution: Standard higher order on a 65x65 Cartesian mesh.

(a) Quadrilateral mesh

(b) 1st order

(c) Multidimensional

(d) Higher order

Figure 8: (a)Unstructured quad-mesh 128 vertices. (b)standard first order method. (c) Multidimensional upwind method. (d) Higher order.

19

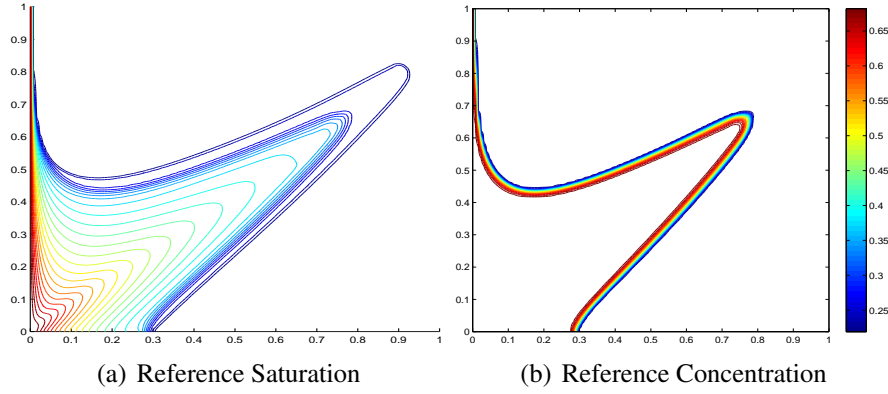(a) Reference Saturation   (b) Reference Concentration

Figure 9: (a)Reference Solution: Standard higher order on a 256x256 Cartesian mesh.

7.3. CASE 3: High mobility, full-tensor, three-component two-phase system

The three-component two-phase flow test case consists of a polymer flood into an oil filled reservoir, where the injected aqueous phase is comprised of polymer miscible with water. Gravity is not present in this example, which is convection dominant (zero gravity number). Quadratic relative permeabilities are assumed with $\zeta = 2$ and the normalised aqueous viscosity is a function of polymer concentration with $\mu = 0.5 + C$. Injection of polymer miscible with water causes a contact discontinuity to form in aqueous saturation, which terminates the rarefaction, followed by a constant state before a shock.

The test case involves a full homogeneous permeability tensor with a $40 : 1$ anisotropy ratio and principal axes oriented at 45 degrees to the reservoir domain horizontal, which induces strong two-dimensional cross-flow. Water and polymer are injected on the left hand boundary, pressure is specified on the right hand boundary, zero flow solid wall conditions hold on the upper and lower walls. The mobility ratio is set equal to 10. The reference solution on a 256×256 Cartesian grid is shown in Figure 9.

The computed saturation and concentration contours are shown in figures 10 computed at the same reference output time using a 4225 node regular grid, with the prescribed initial data $(S, C) = (0.05, 0.01)$.

The first order results (Figure 10(a),(b)) show smeared front resolution.

The multidimensional results of Figure 10(c),(d) are oscillation free and show a clear improvement of saturation and concentration front resolution in comparison with the first order results (Figure 10(a),(b)). The results show that the saturation and concentration fronts are captured with improved resolution across the grid by the multidimensional method, with significantly reduced cross-wind diffusion when compared to the standard upwind method, and again favor the higher order results in trend.

The higher order method results Figure 10(e),(f) show a dramatic improvement in the resolution of the respective saturation concentration contours, where the expansion fan, contact and shock are clearly visible.
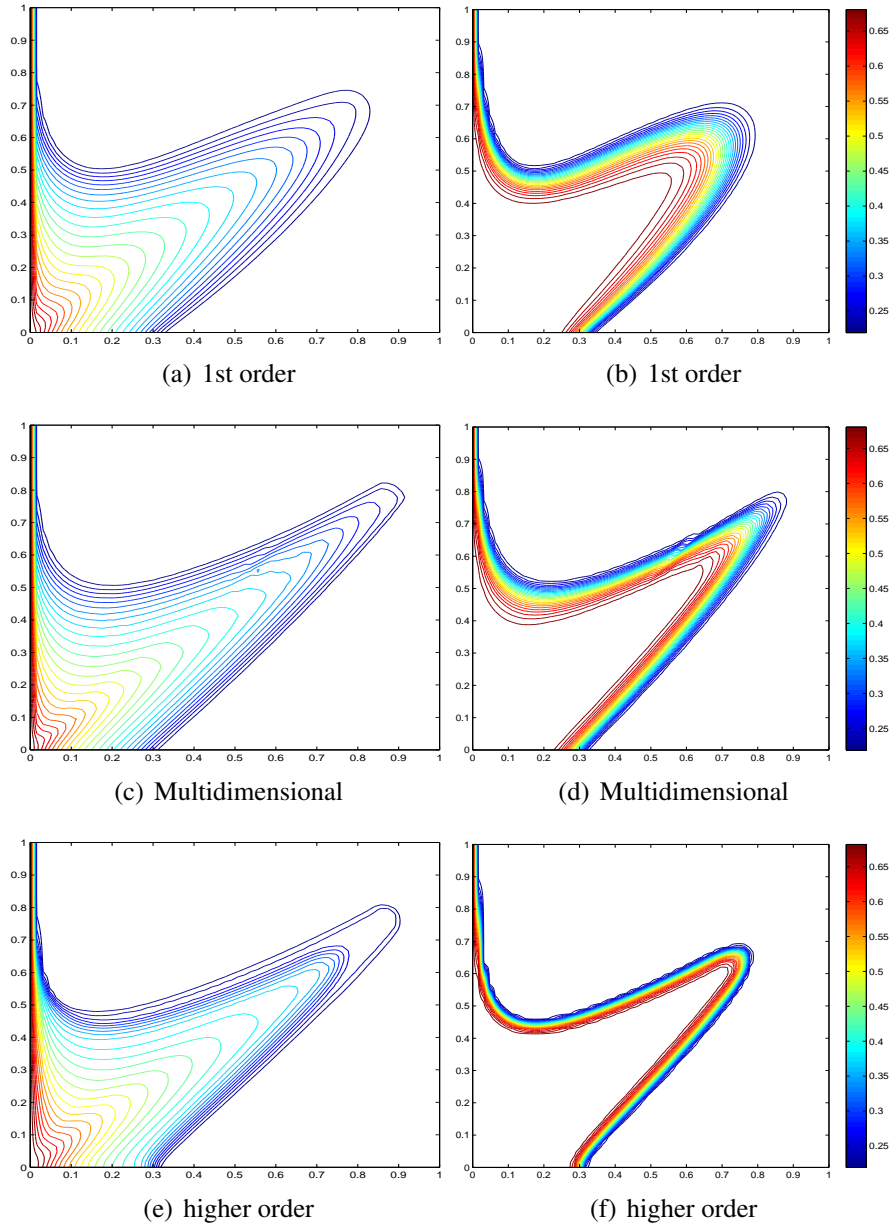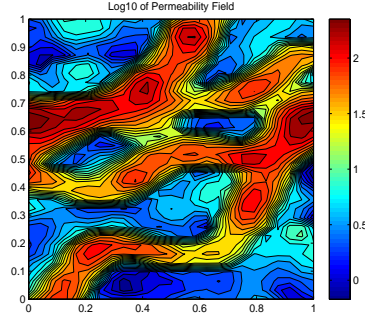
20

Figure 10: (a) standard first order saturation. (b) standard first order concentration.(c) Multidimensional saturation. (d) Multidimensional concentration. (e) higher order saturation. (f) higher order concentration.

(a)

Figure 11: Heterogeneous permeability field.

7.4. CASE 4: Heterogeneous domain with meandering channels, three component two-phase system

The next three-component two-phase flow test case consists of a polymer flood into an oil filled reservoir, where the injected aqueous phase is comprised of polymer miscible with water. As in the previous case gravity is not present in this example, which is convection dominant (zero gravity number). Quadratic relative permeabilities are assumed with $\zeta = 2$ and the normalised aqueous viscosity is a function of polymer concentration with $\mu = 0.5 + C$.

This test case involves a full heterogeneous permeability field with meandering channels across the reservoir domain [43] shown in Fig. 11. Water and polymer are injected on the left hand boundary, pressure is specified on the right hand boundary, zero flow solid wall conditions hold on the upper and lower walls. The mobility ratio is set equal to 100. High mobility ratios lead to shallow shock profiles with a much longer expansion regions.

The computed saturation and concentration contours are shown in figures 12 computed at the same reference output time using a 800 node regular grid, with the prescribed initial data $(S, C) = (0.01, 0.01)$. The first order results (Figure 12(a),(b)) show the most smearing in resolution of the saturation and concentration fronts along the channels .

The multidimensional results of Figure 12(c),(d) show more advanced saturation and concentration fronts along the channels when compared to the first order results (Figure 12(a),(b)). Together with the more advanced front positions, the multidimensional results indicate slightly less spreading across the high permeability channels, which favors the higher order results in trend.

The higher order method results Figure 12(e),(f) show clearer resolution of the respective saturation and concentration contours, indicating that the fronts primarily advance along the high permeability channels.

7.5. CASE 5: Gravity driven three-component two-phase system

A gravity driven three-component two-phase flow system is considered. Initial conditions consist of an aqueous phase comprised of polymer miscible with water sitting on top of oil in an idealized square domain $[0, 1] \times [0, 1]$ with the fluid interface above a solid horizontal shale barrier in the middle of the domain at $y = 0.5$ with lateral extent $0.5 \leq x \leq 1$, which extends halfway across the domain. Solid wall boundary conditions apply at the side and upper boundaries and
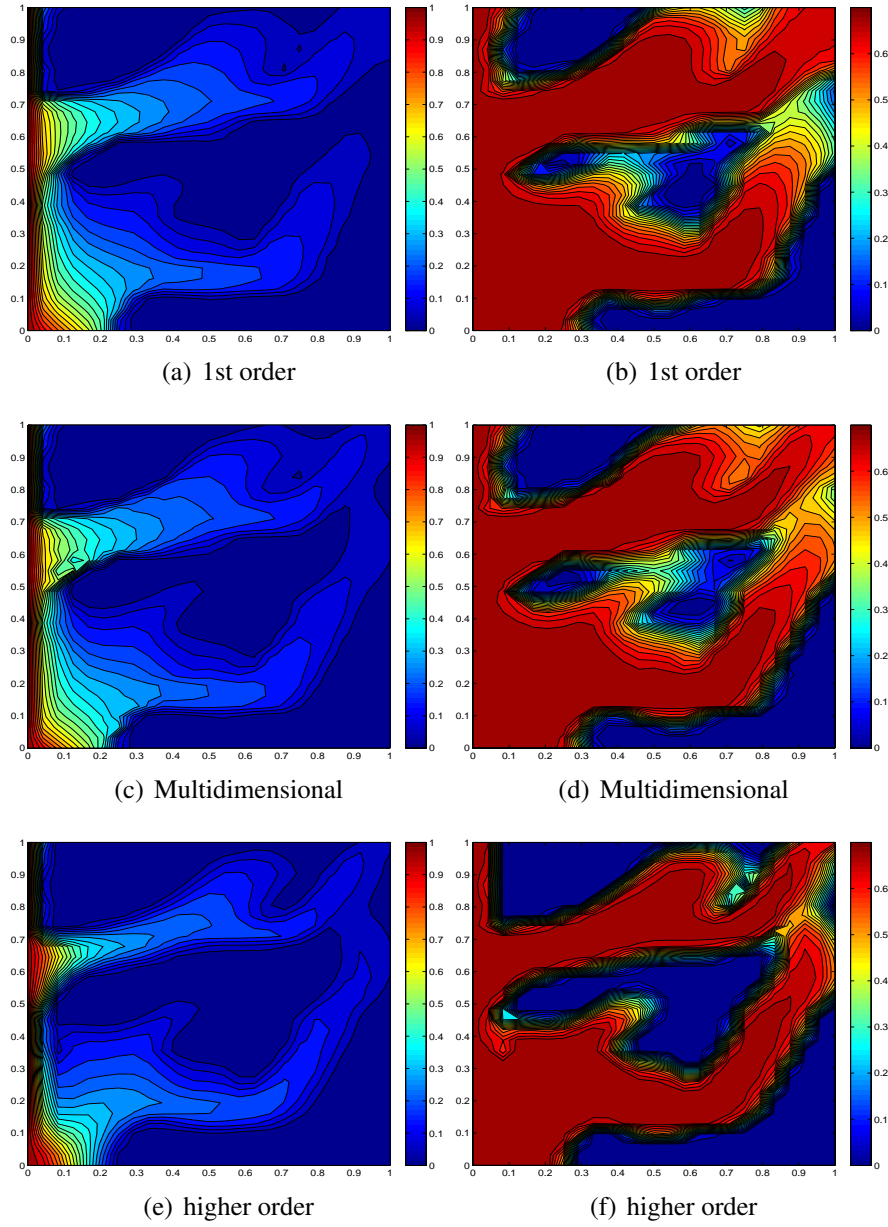
Figure 12: (a) standard first order saturation. (b) standard first order concentration. (c) Multidimensional saturation. (d) Multidimensional concentration. (e) higher order saturation. (f) higher order concentration.

pressure is prescribed on the lower boundary.

Saturation and concentration values are specified with the prescribed initial data (shown in Fig. 13

$$\begin{cases} S, C = 0.2, 0.2, & y \leq 0.7; \\ S, C = 1.0, 0.7, & \text{otherwise.} \end{cases} \tag{49}$$

Quadratic relative permeabilities are assumed with $\zeta = 2$ and the normalised aqueous viscosity is a function of polymer concentration with $\mu = 0.5 + C$.

The numerical case involves a diagonal homogeneous permeability tensor with mobility ratio set equal to 1.

We note that if the shale barrier is absent, the problem is one-dimensional with infinite gravity number. The barrier induces two dimensional flow in an otherwise infinite gravity number problem, posing a major challenge to any scheme proposed for solving a system of essentially hyperbolic transport equations with reverse flow. Consequently the flow solver must be entropy satisfying and be able to resolve rarefactions, shocks and concentration discontinuities.

All water saturation and concentration contours are shown at the same output time 0.5 PVI. A CFL of 0.6 is used for the first order method. The time step is reduced by a factor 2 for higher order results.

The reference solution is computed on a 128x128 Cartesian grid is shown in Figure 15. The nature of the reference solution fronts is carefully noted in making the comparisons between the methods and corresponding conclusions below. Results are shown on an unstructured triangular grid (coarse grid 1060 nodes) and regular 4225 node triangular grid (fine grid) shown in Figure 14.

Standard first order results on the unstructured grids show a smeared front Figure 16(a,b), and distortion of the concentration front due to the grid orientation effects caused by cross-wind diffusion. The cell based multi-dimensional flux formulation is employed with characteristic upwind tracing and primitive variable reconstruction. The multidimensional cell-based tracing results Figure 16(c,d), are free of spurious oscillations and improve resolution of the respective water saturation expansion fan and shock, particularly around the leading edge of the front, with similar improvement in concentration front resolution in comparison with the standard first order results (Figure 16(a,b)). Finer grid results show that the standard first order scheme results improve under refinement Figure 17(a,b). Again flow resolution is improved by the multi-dimensional scheme Figure 17(c,d) (on the same finer grid) relative to the standard first order results of Figure 17(a,b). While both methods are formally first order accurate, the multi-dimensional upwind results indicate improved resolution of fluid fronts relative to the standard first order upwind method on a given grid, indicating that reduced cross-wind diffusion is achieved by the multi-dimensional scheme for a given grid level.

Higher order scheme results are shown Figure 18 computed using the Fromm limiter. While the higher order scheme provides sharper resolution of the saturation and concentration fields, the comparison between the three schemes (standard first order upwind, multidimensional upwind, higher order upwind c.f. Figures 16,17,18) shows that the multidimensional results exhibit similar trends in improved resolution to that of the higher order results. This is particularly note worthy since the multidimensional schemes do not depend on the extended support and slope limiters that form a crucial part of the higher order method.
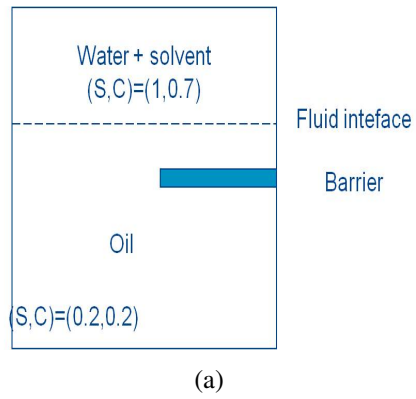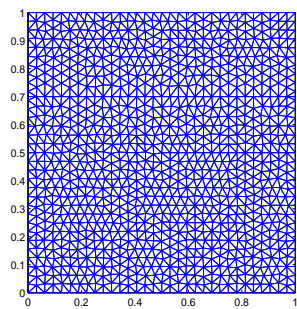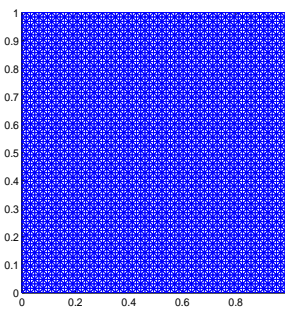
(a)

Figure 13: Heterogeneous permeability field.

(a) 1060 nodes and 1988 cells

(b) 4225 nodes and 8192 cells

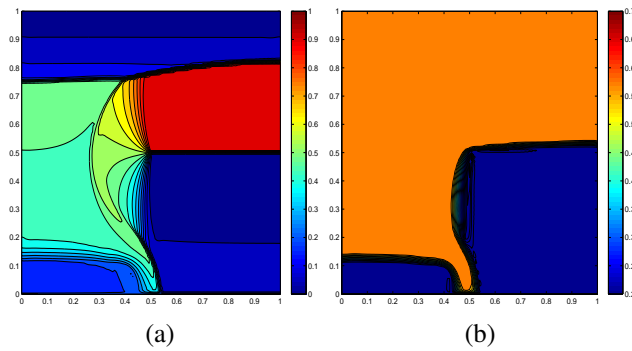Figure 14: Coarse (left) and Fine (right) unstructured triangle grids.

25

Figure 15: Reference solution, 128x128 Cartesian grid . (a) Saturation profile; (b) concentration profile.

8. Conclusions

Both multidimensional upwind cell-based tracing schemes and higher resolution methods have been developed for solving three-component two phase flow systems of conservation laws in porous media on structured and unstructured grids. The methods are applied to two-phase flow and three-component two-phase flow problems including gravity driven flow problems. Comparisons with the standard first order method (single point upstream weighting) are made on structured grids and on triangular and quadrilateral unstructured grids. The multidimensional cell-based tracing schemes provide improved resolution of the saturation fields and concentration fronts in each case, with varying degrees of success according to the problem and grid used.

While the fundamental multidimensional upwind method remains formally first order accurate, the distinction from the standard first order upwind method is in the design of the approximation to capture cross-flow. The multidimensional results show that the method is increasingly effective with increase in strength of cross-flow, which is confirmed by case 3 which has the maximum cross-flow of the five cases presented, and in that sense the results are self-consistent.

The higher order schemes yield results with a significant improvement in resolution of the saturation fields and concentration fronts relative to the standard first order method, except for very coarse grids where the improvement is less pronounced. Comparisons are also made between the multidimensional method and the higher order method results. While the higher order schemes provide sharper resolution, the improved results achieved by the multidimensional schemes exhibit similar trends to the higher order results and it is noted that the multidimensional schemes do not depend on the extended support and slope limiters that form crucial components of the higher order method.

[1] I. Aavatsmark. Introduction to multipoint flux approximation for quadrilateral grids. *Comput.Geo*, 6:405–432, 2002.

[2] R. Abgrall. Toward the ultimate conservative scheme: following the quest. *Journal of Computational Physics*, 167(2):277–315, 2001.

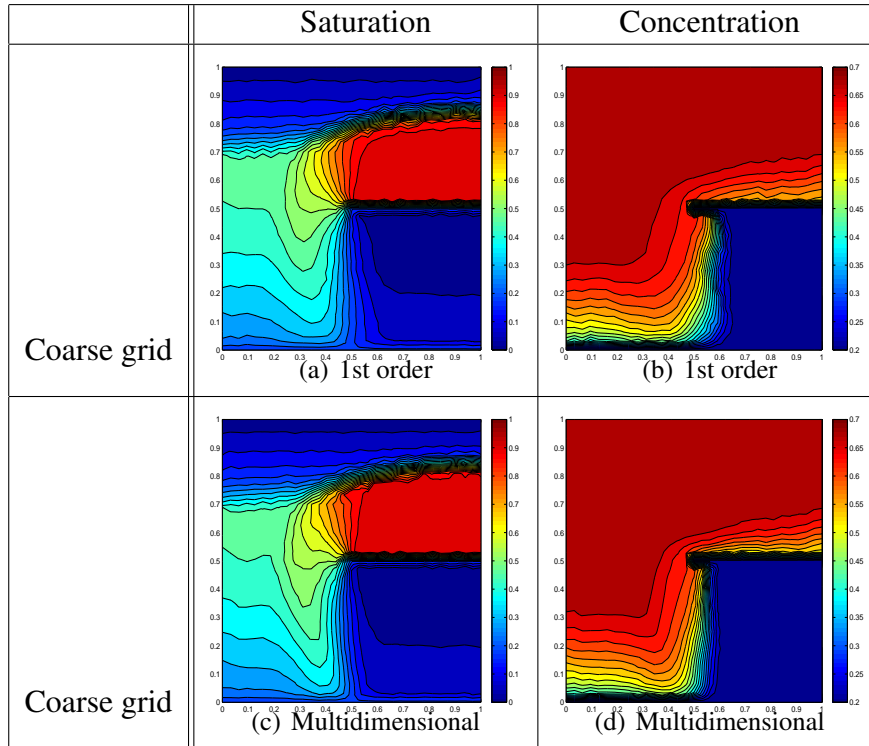[3] K. Aziz and A. Settari. *Petroleum Reservoir Simulation*. Applied Science Publishers, London, 1979.

	Saturation	Concentration
Coarse grid	(a) 1st order	(b) 1st order
Coarse grid	(c) Multidimensional	(d) Multidimensional

Figure 16: Saturation and concentration solutions: (a and b)standard first order scheme. (c and d) Multidimensional scheme

[4] T.J. Barth and M. Ohlberger. *Finite Volume Methods: Foundation and Analysis, Encyclopdeia of Computational Mechanics.* John Wiley and Sons, 2004.

[5] J. Bear. *Dynamics of Fluids in Porous Media.* Elsevier, New York, 1988.

[6] J. B. Bell, P. Colella, and J.A. Trangenstein. Higher order godunov methods for general systems of hyperbolic conservation laws. *Journal of Computational Physics*, 82(2):362–397, 1989.

[7] C. Berger, M.J.and Helzel and R.J. LeVeque. H-box methods for the approximation of hyperbolic conservation laws on irregular grids. *SIAM Journal on Numerical Analysis*, 41(3):893–918, 2003.

[8] M.J. Blunt and B. Rubin. Implicit flux-limiting schemes for petroleum reservoir simulation. *Journal of Computational Physics*, 102:194–210, 1992.

[9] B. Cockburn and C-W. Shu. The runge-kutta discontinuous galerkin finite element method for conservation laws v: Multidimensional systems. *Journal of Computational Physics*, (141):199–224, 1998.

[10] P. Colella. Multidimensional upwind methods for hyperbolic conservation laws. *Journal of Computational Physics*, 87(1):171–200, 1990.
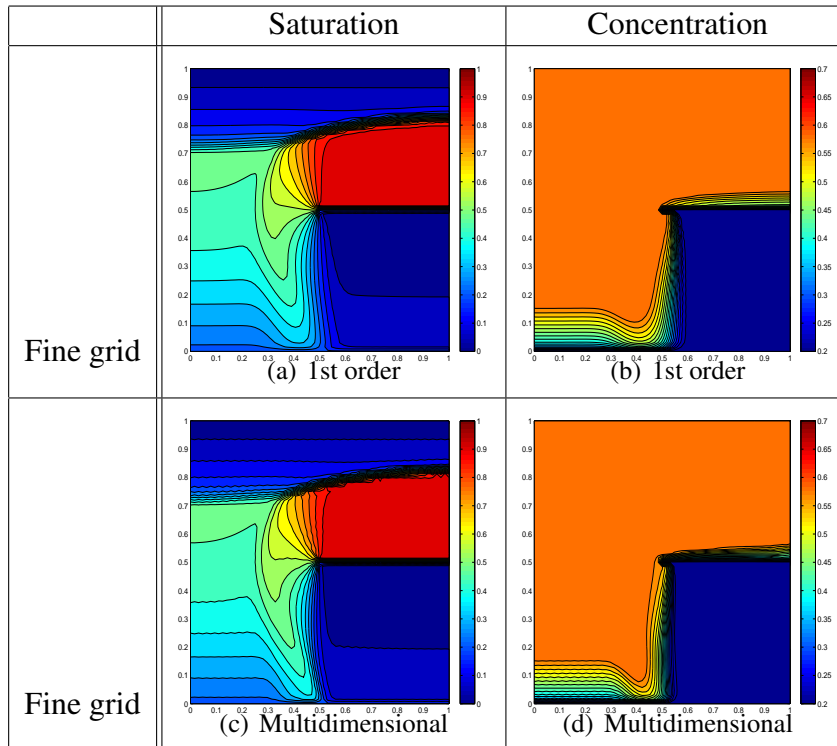
Figure 17: Saturation and concentration solutions: (a and b)standard first order scheme. (c and d) Multidimensional scheme
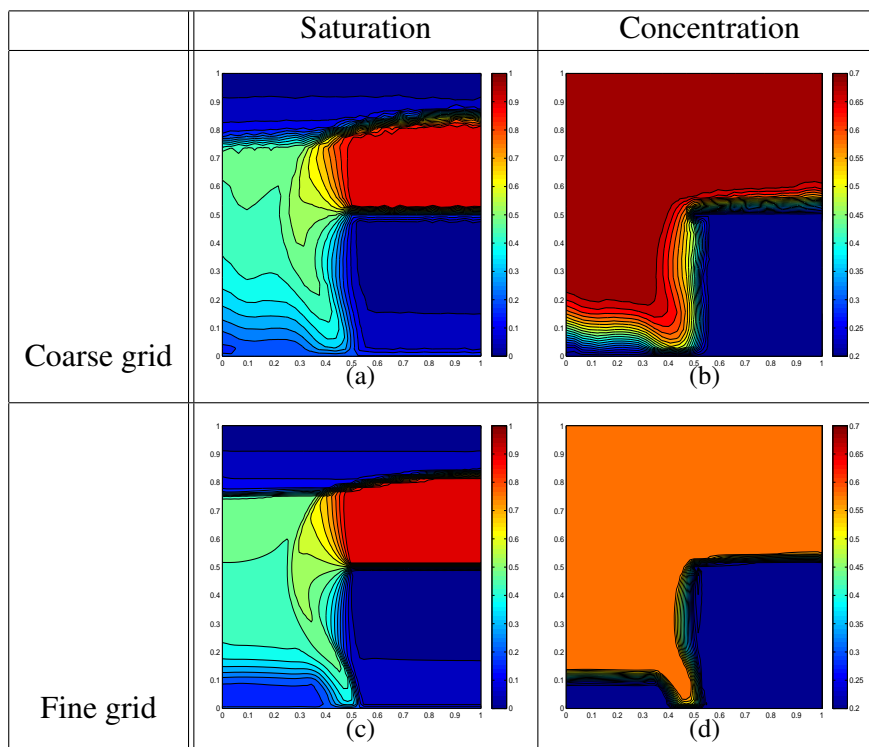

Figure 18: Higher Order saturation and concentration profiles.

[11] C. Dawson, S. Sun, and M.F. Wheeler. Compatible algorithms for coupled flow and transport. *Computer Methods in Applied Mechanics and Engineering*, 193:2565–2580, 2004.

[12] L.J. Durlofsky. A triangle based mixed finite element finite volume technique for modeling two phase flow through porous media. *J.Comput.Phys*, 105:252–226, April 1993.

[13] M.G. Edwards. A higher order godunov scheme coupled with dynamic local grid refinement for flow in a porous medium. *Comput. Methods. Appl. Mech. Engrg*, (131):287 – 308, 1996.

[14] M.G. Edwards. Unstructured, control-volume distributed, full-tensor finite-volume schemes with flow based grids. *Computational Geosciences*, 6:433–452, 2002.

[15] M.G. Edwards. Higher dimensional wave oriented upwind schemes with minimal cross-wind diffusion, spe 79689. In *SPE Reservoir Simulation Symposium*, Houston, Texas, USA, 3-5 Feb 2003.

[16] M.G. Edwards. Higher-resolution hyperbolic-coupled-elliptic flux-continuous cvd schemes on structured and unstructured grids in 2-d. *International Journal for Numerical Methods in Fluids*, 51(9-10):1059 – 1077, 2006.

[17] M.G. Edwards. Global and local central non-upwind finite volume schemes for hyperbolic conservation laws in porous media. *International Journal for Numerical Methods in Fluids*, 64(7):793–811, 2010.

[18] M.G. Edwards. Multi-dimensional wave-oriented upwind schemes with reduced cross-wind diffusion for flow in porous media. *International Journal for Numerical Methods in Fluids*, 67(1):33–57, 2011.

[19] M.G. Edwards and M.A. Christie. Dynamically adaptive godunov schemes with renormalization for reservoir simulation, spe 25268. In *Twelfth SPE Reservoir Simulation Symposium*, New Orleans, Louisiana, USA, Feb 28-Mar 3 1993.

[20] M.G. Edwards and H. Zheng. Double-families of quasi-positive darcy-flux approximations with highly anisotropic tensors on structured and unstructured grids. *Journal of Computational Physics*, 229:594–625, 2010.

[21] E. Godlewski and P.A. Raviart. *Numerical approximation of hyperbolic systems of conservation laws*. New York, Springer, 1996.

[22] C. Helzel, M.J. Berger, and R.J. LeVeque. A high-resolution rotated grid method for conservation laws with embedded geometries. *SIAM Journal on Scientific Computing*, 26(3):785–809, 2005.

[23] Ch. Hirsch and P. van Ransbeek. Cell centered multidimensional upwind algorithm and structured meshes. In Elsevier, editor, *Proceedings of ECOMAS 1st European CFD Conference*, volume 1, pages 53–60, Amsterdam, The Netherlands, 1992.

[24] H. Hoteit and A. Firoozabadi. Compositional modeling by the combined discontinuous galerkin and mixed methods. *SPE J.*, 11(1):19–34, March 2006.

[25] M.E. Hubbard and M.J. Baines. Conservative multidimensional upwinding for the steady two-dimensional shallow water equations. *Journal of Computational Physics*, 138(2):419–448, 1997.

[26] A. Jameson. Analysis and design of numerical schemes for gas dynamics 1, artificial diffusion, upwind biasing, limiters and their effect on multigrid convergence. *Int. J. of Comp. Fluid Dyn*, 4:171–218, 1995.

[27] E. Keilegavlen, J. Kozdon, and B. Mallison. Multidimensional upstream weighting for multiphase transport on general grids. *Comput Geosci*, 16:10211042, 2012.

[28] J. Kozdon, B. Mallison, and M. Gerritsen. Robust multi-d transport schemes with reduced grid orientation effects. In *Reservoir Simulation Symposium SPE 119190, Houston TX USA, Feb 2009*.

[29] M.S. Lamine and M.G. Edwards. Higher dimensional upwind schemes for flow in porous media on unstructured grids. In *ECMOR XI, 11th European Conference on the Mathematics of Oil Recovery*, Bergen, Norway, 8 - 11 September 2008.

[30] S. Lamine and M.G. Edwards. Higher-resolution convection schemes for flow in porous media on highly distorted unstructured grids. *International Journal for Numerical Methods in Engineering*, 76(8):1139–1158, 2008.

[31] S. Lamine and M.G. Edwards. Higher order multidimensional upwind convection schemes for flow in porous media on structured and unstructured quadrilateral grids. *SIAM J. Sci. Comput.*, 32:1119–1139, 2010.

[32] S. Lamine and M.G. Edwards. Multidimensional upwind convection schemes for flow in porous media on structured and unstructured quadrilateral grids. *Journal of Computational and Applied Mathematics*, 234(7):2106–2117, 2010.

[33] S. Lamine and M.G. Edwards. Higher order cell-based multidimensional upwind schemes for flow in porous media on unstructured grids. *Comput. Methods Appl. Mech. Engrg.*, 259:103122, 2013.

[34] S. H. Lee, L. Durlofsky, M. Lough, and W. Chen. Finite difference simulation of geologically complex reservoirs with tensor permeabilities. *SPERes.Engrg*, 1:567–574, 1998.

[35] R.J. Leveque. *Finite Volume Methods for Hyperbolic Problems*. Cambridge University Press-London, 2002.

[36] P.R.M. Lyra and K. Morgan. A review and comparative study of upwind biased schemes for compressible flow computation. part iii: Multidimensional extension on unstructured grids. *Archives of Computational Methods in Engineering*, 9(3):207–256, September 2002.

[37] J. Moortgat, Z. Li, and A. Firoozabadi. Three-phase compositional modeling of co2 injection by higher-order finite element methods with pr and cpa equations of state. *Water Resources Research*, 48, 2012.

[38] J. Moortgat, S. Sun, and A. Firoozabadi. Compositional modeling of three-phase flow with gravity using higher-order finite element methods. *Water Resources Research*, 47, 2011.

[39] M. Pal, M.G. Edwards, and A.R. Lamb. Convergence study of a family of flux-continuous finite schemes for the general tensor pressure equation. *International Journal for Numerical Methods in Fluids*, 51:1177–1203, 2006.

[40] G. D. Raithby. Skew upstream differencing schemes for problems involving fluid flow. *Computer Methods in Applied Mechanics and Engineering*, 9:153–164, October 1976.

[41] B. Riviere and M.F. Wheeler. Discontinuous Galerkin methods for flow and transport problems in porous media. *Communications in Numerical Methods in Engineering*, 18:63–68, 2002.

[42] P. L. Roe and D. Sidilkover. Optimum positive schemes for advection in two and three dimensions. *SIAM Journal of Numerical Analysis*, 29(6):1542–1568, Dec 1992.

[43] P.L. Roe, H. Deconinck, and R.J. Struijs von Karman. Fluctualtion splitting for multidimensional convection problems: An alternative to finite volume and finite element methods. VKI Computational Fluid Dynamics Lecture Series, 03 1990.

[44] P.L. Roe, H. Deconinck, and R.J. Struijs von Karman. Recent progress in multidimensional upwinding. In K. W. Morton, editor, *Numerical Methods in Fluid Dynamics*, volume 371 of *Lecture Notes in Physics, Berlin Springer Verlag*, pages 273–277, 1990.

[45] Mao S. and Journal A.G. Generation of a reference petrophysical data set. The Stanford V Reservoir. Stanford Center for Reservoir Forecasting Report., 1996.

[46] C.W. Shu and S. Osher. Efficient implementation of essentially non-oscillatory shock-capturing schemes,ii. *Journal of Computational Physics*, 83(1):32–78, 1989.

[47] P. K. Smolarkiewicz and Szmelter J. Mpdata: an edge-based unstructured-grid formulation. *Journal of Computational Physics*, 206(2):624–649, 2005.

[48] P.K. Sweby. High resolution schemes using flux limiters for hyperbolic conservation laws. *SIAM Journal on Numerical Analysis*, 21(5):995–1011, October 1984.

[49] M. Thiele and M.G. Edwards. Physically based higher order godunov schemes for reservoir simulation for compositional simulation, spe 66403. In *SPE Reservoir Simulation Symposium*, Houston, Texas, USA, Feb 11-14 2001.

[50] B. van Leer. Towards the ultimate conservative difference scheme, v. a second-order sequel to godunov's method. *J. Comput. Phys.*, 32:101–236, 1979.

[51] M. F. Wheeler, C. N. Dawson, and J. Eaton. Transport of multispecies contaminants with biological and chemical kinetics in porous media. *Modeling and Computation for Applications in Mathematics, Science, and Engineering (Evanston, IL, 1996), Numerical Mathematics and Scientific Computation, Oxford Univ. Press, New York*, pages 25–37, 1998.

[52] M.F. Wheeler and I. Yotov. A Multipoint Flux Mixed Finite Element Method. *Siam Journal on Numerical Analysis*, 44:2082–2106, 2006.